Desalination 600 (2025) 118429

Contents lists available at ScienceDirect

Desalination

journal homepage: www.elsevier.com/locate/desal

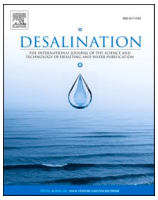

Separation of monovalent salts by reverse osmosis modules: A 2D mass transport model based on solution friction theory

E.M. Kimani [a,b], A.J.B. Kemperman [a,b], S. Porada [a,c], P.M. Biesheuvel [a], W.G.J. van der Meer [b,*]

[a] Wetsus, European Centre of Excellence for Sustainable Water Technology, Oostergoweg 9, 8911 MA Leeuwarden, The Netherlands
[b] Department of Membrane Science and Technology, University of Twente, Drienerlolaan 5, 7522 NB Enschede, The Netherlands
[c] Department of Process Engineering and Technology of Polymeric and Carbon Materials, Wrocław University of Science and Technology, Wybrzeże Stanisława Wyspiańskiego 27, 50-370 Wrocław, Poland

HIGHLIGHTS

- The novel use of solution friction theory in a 2D mass transport model for reverse osmosis (RO) membranes.
- Numerical simulations to evaluate local and overall performance metrics in RO modules
- Effects of hydraulic pressure losses in the feed channel on RO module performance.
- Performance optimization for RO modules through a sensitivity analysis.

GRAPHICAL ABSTRACT

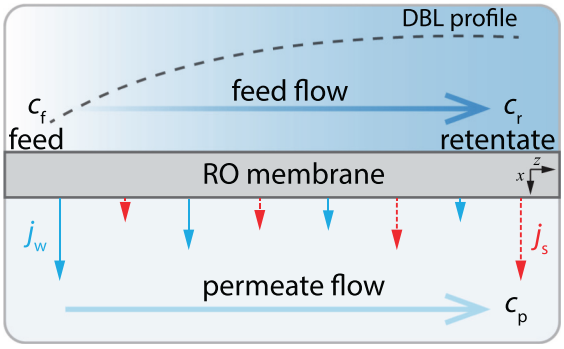

ARTICLE INFO

Keywords:
Mathematical model
Reverse osmosis
2D mass transport
Solution friction theory
Salt rejection

ABSTRACT

Developing a detailed two-dimensional (2D) theoretical framework for mass transport in a spiral wound reverse osmosis (RO) module is crucial to better understand membrane processes. In this study, we developed a 2D mass transport model for a monovalent binary symmetric salt (1:1) using the solution friction theory. Mass and volume balances were used to define cross-flow velocity and salt concentration along the module length. The numerical simulations analyzed local RO module performance, such as fluxes, pressures, axial velocity, mass transfer coefficient, water recovery, and salt rejection. The simulation results demonstrated that hydraulic pressure loss along the module length has a minor effect on a single module's local and overall performance. Conversely, the effect becomes significant when several modules are stacked in a pressure vessel (PV). The performance optimization for brackish water and seawater desalination membranes was conducted using low-salinity feed water (50 mM NaCl). This involved a detailed parametric study on the operational conditions, membrane geometry, and number of module elements in a PV.

* Corresponding author.
E-mail address: w.g.j.vandermeer@utwente.nl (W.G.J. van der Meer).

https://doi.org/10.1016/j.desal.2024.118429
Received 22 August 2024; Received in revised form 7 November 2024; Accepted 16 November 2024
Available online 19 December 2024

1. Introduction

Reverse osmosis (RO) is the most common and efficient pressure-driven membrane technology for water desalination. The RO membrane makes use of its highly cross-linked polyamide (PA) active layer to achieve selectivity towards salts and other contaminants. The high selectivity is achieved through exclusion mechanisms, in which ions are partitioned at the bulk-membrane interface due to the membrane pore (steric), affinity (dielectric), and membrane charge (Donnan) [1–6]. However, when dealing with multi-component mixtures, the selectivity trends of certain species become complex due to ion-ion and ion-membrane matrix interactions [7–9]. Such a knowledge gap has increased efforts to gain an in-depth understanding of transport and separation mechanisms by RO membranes for performance optimization. The development of sophisticated and robust RO mathematical models and incorporating all pertinent physicochemical interactions can enable a more comprehensive understanding of RO processes [10].

Different modeling approaches have been developed for specific applications in mass transport theory for RO membranes. Often, these models are based on a one-dimensional (1D) geometry, in which ion transport occurs only across the thin PA active layer. The widely employed transport theory for 1D models is the extended Donnan steric partitioning pore model (ext-DSPM) [11–14], which uses the extended Nernst-Planck equation (ext-NPE) to describe transport of ions through the membrane thickness [15–17]. The advantage of using this approach is that the ext-DSPM can be further extended to include physical-chemical descriptions such as membrane charge ionization, acid-base reactions, ion pairing, and ion-membrane matrix interactions, etc., and numerically solved [7,9,18–20]. However, the downside of a 1D model is the lack of lateral mass transport predictions, i.e., along the membrane length [21].

To ensure a realistic transport description, two-dimensional (2D) and three-dimensional (3D) models have been developed to include channel flow hydrodynamics, which analyzes fluid flow within a channel of a specified geometry. Extensive work has been done in 2D model description and development, with studies often using the solution-diffusion (SD) theory to describe water and salt mass transport. For instance, work done by Van der Meer and Van Dijk [22] investigated RO module performance by developing a 2D mathematical model using SD theory and included hydraulic pressure variation in the feed and permeate channels. Guillen and Hoek [23] modeled the RO module using SD theory and included the effects of spacer geometry on mass transfer, hydraulic losses, permeate quality, and energy consumption. Most 2D and 3D models are based on computational fluid dynamics (CFD), simulating the effects of spacer geometry and placement on lateral electrolyte flows, which affect the diffusion boundary layer (DBL), and the overall membrane performance [23–29].

Recent studies have also argued that the SD model does not correctly describe water and salt transport mechanisms in RO membranes. Several assumptions used by the SD model have been invalidated through experimental and theoretical studies. For instance, a recent study shows that the driving force of water transport in RO membranes is due to a hydraulic pressure gradient within the membrane and not by diffusion due to the concentration gradient of water within the membrane matrix as assumed by the SD model [30]. This was also confirmed by performing solvent permeation experiments and non-equilibrium molecular dynamics simulations [31]. In another study, small-angle and quasi-elastic neutron scattering were used to show the free movement of water molecules in continuous water channels formed by the membrane polymer matrix. These studies contradict the widely accepted SD model, which assumes that the transport of water molecules is directly associated with polymer dynamics [32]. Several studies have also experimentally and theoretically suggested the presence of convective transport of salt, which is not accounted for in the SD model [33,34]. In addition, experimental observations have argued against using constant partitioning coefficients of water and salt, as is considered by the SD model [35,36]. The critical flaws of the SD model, as highlighted in [37], point to a fundamental misunderstanding of water transport mechanisms in RO membranes. This work underscores the necessity for a critical reevaluation of the assumptions underlying the SD model to enhance its applicability and accuracy in predicting RO membrane performance.

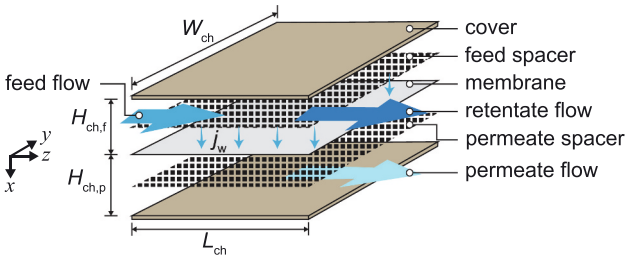

Fig. 1. Detailed geometrical depictions of RO module with an unwound membrane sheet and spacers.

It is also important to point out that the modeling of RO processes can be highly intricate and requires detailed information that is often challenging to obtain experimentally in full-scale desalination plants. As a result, this complexity has driven the adoption of machine learning-based models for parameter estimation in reverse osmosis systems. These hybrid models leverage both mechanistic and data-driven techniques to estimate important parameters, enhancing the predictive accuracy and efficiency of the RO process simulations and overcoming the limitations of traditional experimental methods [10,38–46].

In this study, we present an in-depth yet simple numerical 2D mass transport model based on the solution friction (SF) theory as derived by Biesheuvel et al., [47] to investigate the desalination of monovalent cation and anion binary salt (NaCl) by an RO module with a defined effective membrane active surface area (A_m). We compare two cases: one with pressure loss along the module length in the feed channel and one without. In both cases, flows in the permeate channel were excluded, leading to an assumption that the hydraulic pressure in the permeate channel remained constant.

The primary objective of this study extends beyond the analysis of the overall module performance and explores the theoretical basis of mass transport at localized points along the module's length. This includes a study of the resultant local axial fluxes of water and salt alongside considerations of salt rejection, water recovery, and pressure differences. Furthermore, using low salinity feedwater (50 mM NaCl), performance optimization is conducted on a membrane for brackish water desalination (BWM) and a membrane for seawater desalination (SWM) through a comprehensive parametric study. By systematically varying the process conditions, we evaluate our theoretical predictions and determine the optimal operational parameters necessary to meet the specified produced water requirements.

2. Theory

In this section, we develop a simplified yet comprehensive 2D mass transport model for 1:1 binary salt using the solution-friction (SF) theory. The theory is based on the “sieving“effect as described by Spiegler and Kedem [48], in which friction factors between ions (solutes) and the membrane (sieve) are defined. A single RO membrane module can be represented simply by two filtration channels (feed and permeate) with the membrane in between. For a spiral-wound reverse osmosis (SWRO) module, the flow channels can be assumed to be rectangular and formed by unwrapping the SWRO elements into a flat sheet membrane. The channel length, width, and height are represented by L_{ch}, W_{ch}, and H_{ch}, respectively. A detailed geometrical depiction of our modeling approach with parametric components of an RO module with an unwound membrane sheet and spacers is depicted in Fig. 1.

2.1. Model description

The developed model is based on a few premises and assumptions. First, the salt mass transport through the membrane active layer (x-direction) is considered to be predominantly diffusive (concentration gradient) and electromigrative (potential gradient). In contrast, salt mass transport along the membrane module (z-direction) is strictly convective (flow with solvent).

The membrane geometric properties are incorporated by porosity, ρ, and tortuosity, τ. Moreover, the membrane is characterized by a constant volumetric charge density, X_m.

We consider a 1:1 binary salt with a monovalent cation and anion. The ionic species are not involved in chemical reactions in any flow direction. They are described by a harmonic mean diffusion coefficient, $D_{\infty,s}$, a uniform friction factor between the species and the membrane matrix, $K_{f,s}$, and identical mass transport coefficient within the diffusion boundary layer (DBL), $k_{DBL,s}$ and inside the membrane, $k_{m,s}$, ensuring symmetry in their behavior.

Ultimately, we assume that the electrolyte solution is uniformly mixed throughout the transverse direction of the channel. With this assumption in effect, the governing equations in one spatial dimension are deemed adequate.

2.2. Governing equations

2.2.1. Solute transport across the membrane

The derivation of the salt transport starts with the ext-NPE evaluating ionic flux through the membrane. With our earlier stated assumption that salt mass transport across the membrane thickness is dominated by diffusion and electromigration, the ionic flux, j_i, is then given by

$$j_i = -K_{f,i}\varepsilon_m D_{\infty,i}\left(\frac{\partial c_i}{\partial x} + z_i c_i \frac{\partial \phi}{\partial x}\right), \tag{1}$$

where $D_{\infty,i}$ is the bulk diffusion coefficient of an ionic species i, $K_{f,i}$ is the friction factor between the ion and the membrane matrix, ε_m is the mass transport reduction factor given by $\varepsilon_m = p/\tau$, where p is the porosity, and τ is the pore tortuosity, z_i and c_i are species valence and concentration respectively, x is the position coordinate across the membrane thickness, δ_m, and ϕ is the dimensionless electrical potential scaled by RT/F, where R is the universal gas constant, T is the temperature in K, and F is Faraday constant.

For RO membranes, taking into account the assumptions above (thus dropping out the index i and using S for salt), we can combine Eq. (1) with local charge electroneutrality ($c_+ + c_- + X_m = 0$) and zero current ($j_+ - j_- = 0$), and derive the salt flux equation. Following a series of numerical, analytical, and integral solutions as explained in detail by Biesheuvel et al. [47], the salt flux is expressed as

$$j_s = P_s\left(\sqrt{C^2 + c_{int}^2} - \sqrt{C^2 + c_p^2}\right), \tag{2}$$

where c_{int} and c_p are the salt concentrations on the feed-membrane interface and the permeate stream respectively, P_s is the salt transport factor given by $P_s = K_{f,s}\Phi_s k_{m,s}$, where Φ_s is the salt partitioning coefficient, and $k_{m,s}$ given by $k_{m,s} = D_{\infty,s}\varepsilon_m/\delta_m$. C is the charge factor in mM and given by $C = \frac{|X_m|}{2\Phi_s}$ where $|X_m|$ is the absolute membrane charge density in mM.

The diffusion boundary layer (DBL) is included in the membrane transport model, in which the salt concentration on the feed-membrane interface is given by

$$c_{int} = \frac{j_s}{j_w} + \left(c_f - \frac{j_s}{j_w}\right) exp\left(\frac{j_w}{k_{DBL,s}}\right), \tag{3}$$

where j_w is the trans-membrane water flux in L/m^2/h (LMH), and $k_{DBL,s}$ is the solute mass transfer coefficient in the DBL and can be approximated by means of dimensionless numbers using the Sherwood correlation for laminar flow in thin rectangular channels. All the parameters in Eq. (3) are z-directional dependent. Previous studies have shown that $k_{DBL,s}$ starts at an infinite value at the inlet of the feed channel and drops to lower values along the channel towards the channel outlet (retentate side) [49]. The relation for this reduction is given by [50].

$$k_{DBL,s}(z) = \alpha\left[\frac{D_{\infty,s}^2\gamma}{z}\right]^{1/3}, \tag{4}$$

where z is the directional-coordinate along the channel length from the inlet (feed side) i.e., $z = 0$, to the outlet (retentate side) i.e., $z = L_{ch}$, α is a dimensionless coefficient and estimated to be $\alpha = 0.662$ [50], γ is the shear rate due to solvent cross-flow (axial) velocity change in x-direction, $\partial v_z/\partial x$, and is given by $\gamma = 6v_z/H_{ch}$. The shear rate equation assumes the fluid is non-compressible and the flow is unidirectional.

2.2.2. Solvent transport across the membrane

Solvent flow drives solute transport across and along the membrane through convective flow. In one-dimensional models, this flow is at times referred to as trans-membrane water flux (j_w) or trans-membrane water velocity (v_f). It is either an imposed value or computed by the force balance between applied pressure, osmotic pressure, and friction with the membrane and potentially with ions. However, in 2D modeling, water flux acts in two directions; across the feed channel (v_x) and along the module length (v_z).

The water flux across the membrane, j_w, as expressed by Kedem and Katchalsky [33], is given by

$$j_w = A_w(\Delta P_h - \sigma'\Delta\Pi), \tag{5}$$

where A_w is the membrane water permeability coefficient (LMH/bar), ΔP_h is the transmembrane hydraulic pressure (bar) given by $\Delta P_h = P_{st} +$ TMP (P_{st} is the static pressure and TMP is the transmembrane pressure), $\Delta\Pi$ is the transmembrane osmotic pressure (bar), and σ' is the salt reflection coefficient for charged membranes which depends on the membrane and salt properties [47].

As described in ref. [47], the reflection coefficient for charged membranes, σ' is given by $\sigma' = 1 - (1 - \sigma)f$, where σ is the classical reflection coefficient defined as $\sigma = 1 - K_{f,s}\Phi_s$ and f is a function which equates to unity for uncharged membranes, thus resulting to $\sigma'=\sigma$. For charged membranes, f is defined as $f = \sqrt{(C/c_{int})^2 + 1} - C/c_{int}$. Due to the ideal selectivity of RO to solvent [51], the classical reflection coefficient, σ, will be close to unity. When a charged membrane is considered, $\sigma'>\sigma$, but still closer to unity [47]. Therefore, we also set $\sigma' = 1$ in this study.

By including the DBL, then $\Delta\Pi$ is the difference between the osmotic pressure at the membrane interface on the feed side (Π_{int}) and that on the permeate side (Π_p), and expressed as

$$\Delta\Pi = \Pi_{int} - \Pi_p = 2RT(c_{int} - c_p), \tag{6}$$

where R is the gas constant, T is the temperature in K, c_{int} and c_p are the solute concentrations on the membrane interface and permeate, respectively.

2.2.3. Transport through flow channels

Transport along the membrane (z-direction) happens through spacer channels, which are thin and long channels next to the membrane either on the feed or the permeate sides. The transport is assumed to be predominantly convective since the length of the flow channel is very long, and therefore, in this flow direction, convection is by far the most important transport mechanism. We use a plug flow regime to describe transport in z-direction, meaning that the solvent velocity component in z-direction is independent of x. To derive mass transport components in the flow channels, we must set up differential mass and volume balances

in the feed and permeate channels, as explained below.

(a) *Balances in the feed channel*

The feed channel is on the upstream side of the membrane where the salt solution flows. Since the mass transport in the feed channel is mainly by convection, the mass balance is defined as

$$\rho_{s,f}\frac{\partial c_f}{\partial t} = -\frac{\partial(c_f v_z)}{\partial z} - \frac{j_s}{H_{ch,f}}, \tag{7}$$

where $\rho_{s,f}$ is the feed spacer porosity, c_f is the feed concentration, v_z is the flow velocity in z-direction (cross-flow velocity), $H_{ch,f}$ is the feed channel height (feed spacer thickness) as shown in Fig. 1.

With an assumption of a steady state system (time-independent) and expressing v_z as a function of feed volumetric flow rate (Q_f), we can re-write Eq. (7) to express the salt flux transport along the channel and given by

$$j_s = -\frac{\partial(c_f v_z)}{\partial z}H_{ch,f} = -\frac{1}{W_{ch}}\frac{\partial(c_f Q_f)}{\partial z}. \tag{8}$$

The volume balance in the feed channel is evaluated where both transversal (v_x) and axial (v_z) fluid flows are defined. The two velocities are a function of the local position in their respective flow directions, i.e., the x-direction and z-direction. The flow in x-direction increases from v_x=0, at the back of the module casing (cover in Fig. 1), to $v_x = j_w$ at the feed-membrane interface. Since volume does not accumulate, the volume balance across the channel (x-direction) on the upstream (feed) side is given by

$$\frac{\partial v_x}{\partial x} = -\frac{j_w}{F_c H_{ch,f}}, \tag{9}$$

where F_c is the water flux conversion factor, i.e., from LMH to m/s ($F_c = 3.6 \times 10^6$). Similarly, v_z decreases from $v_z = v_{in}$ to $v_z = v_{out}$ and is given by

$$\frac{\partial v_z}{\partial z} = \frac{1}{A_{ch}}\frac{\partial Q_f}{\partial z} = -\frac{j_w}{F_c H_{ch,f}}, \tag{10}$$

where A_{ch} is the channel cross-sectional area given by $A_{ch} = W_{ch} \times H_{ch,f}$. In this study, we assume that v_z is not affected by the irregularity of the membrane active layer morphology, as was investigated by [52].

Integrating Eq. (10) with respect to ∂z and setting the limits to $z = 0$ and $z = L_{ch}$ gives

$$v_z - v_0 = -\frac{1}{F_c H_{ch}}\int_0^z j_w dz, \tag{11}$$

where v_0 is the initial cross-flow velocity at the entrance of the module and is given by $v_0 = Q_f/A_{ch}$.

(b) *Balances in the permeate channel*

On the permeate side, we evaluate mass and volume balances by simply inverting the signs for the trans-membrane water flux (j_w) and the salt flux, (j_s) in z-direction, i.e.,

$$\frac{\partial v_x}{\partial x} = \frac{j_w}{F_c H_{ch,p}}, \tag{12}$$

and

$$\rho_{s,p}\frac{\partial c_p}{\partial t} = \frac{\partial(c_p v_z)}{\partial z} + \frac{j_s}{H_{ch,p}}, \tag{13}$$

where $\rho_{s,p}$ is the permeate spacer porosity, and $H_{ch,p}$ is the permeate channel height.

We also assume a constant hydraulic pressure in the permeate channel, thus neglecting the pressure drop along the channel length, i.e., $P_{h,p}(z) = \text{constant} = 0$ bar.

2.3. Modeling cases

2.3.1. Case I: axial pressure gradient neglected

In this case, we assume that the axial hydraulic pressure gradient is insignificant and, therefore, neglected. For the entire membrane length, L_{ch}, we assume the same hydraulic pressure difference, ΔP_h, across the membrane.

2.3.2. Case II: axial pressure gradient included

For case II, the axial hydraulic pressure gradient is included in the model. The drop of the TMP along the membrane length (z-direction) is given by [24,53,54].

$$\frac{\partial P_h}{\partial z} = -k\frac{12 v_z \eta}{P_c H_{ch}^2}, \tag{14}$$

where η is the solution dynamic viscosity, P_c is the pressure conversion factor, i.e., from Pa to bar ($P_c = 10^5$), and k is the friction coefficient due to spacer geometry and assumed to be $k \geq 1$ [55]. Although it is well-established that the feed spacer geometry influences both the

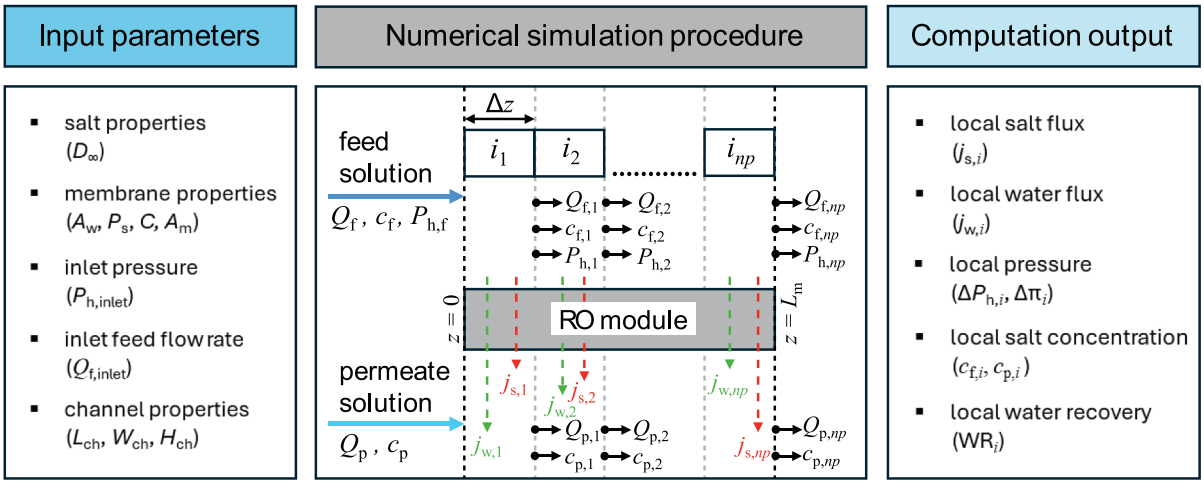

Fig. 2. The RO process simulation followed when solving differential and algebraic equations. The model simulation gives the local prediction for all *np* segments.

Table 1
Default case study conditions unless otherwise stated.

Feed properties		
Salt concentration $c_{f,NaCl}$	50 mM	
Bulk salt diffusivity, $D_{\infty,NaCl}$	$1.64 \times 10^{-9}\ \frac{m^2}{s}$	
Reference temperature, T_{ref}	25 °C	
Dynamic viscosity, η	0.895 mPa·s	
Feed channel hydrodynamics		
Channel height, H_{ch}	711 μm	
Channel length, L_{ch}	1 m	
Channel width, W_{ch}	1 m	
Friction coefficient, k	7 [24]	

Membrane properties (from Ref. [47])		
Membrane active area, A_m	$1\ m^2$	
	BWM	SWM
Water permeability, A_w ($\frac{LMH}{bar}$)	3.3	2.2
Transport factor, P_{NaCl} (LMH)	0.72	0.39
Charge factor, C (mM)	0	55

hydraulic pressure drop and the mass transfer coefficient in the DBL [56–62], this study did not explore these effects in detail, as they were outside the scope of the current investigation. Similarly, the effect of membrane fouling on pressure drop as investigated in ref. [55] was not included in this study. If we integrate Eq. (14) along z-direction and assume that pressure in the permeate channel is the same along the module length, we arrive at

$$\Delta P_{h,z} - \Delta P_{h,0} = -k\frac{12\eta}{P_c H_{ch}^2}\int_0^z v_z \partial z, \tag{15}$$

where $\Delta P_{h,0}$ is the initial TMP at the entrance of the module. The friction coefficient, k, is determined by integrating Eq. (14) with boundary limits set to $z = 0$ and $z = L_{ch}$ and expressed as

$$k = \frac{P_c H_{ch}^2}{12 v_0 \eta L_{ch}}\left(\Delta P_{h,0} - \Delta P_{h,L_{ch}}\right), \tag{16}$$

where $\Delta P_{h,L_{ch}}$ is the TMP at the exit of the module. Eq. (16) is a simplified version that makes use of the assumption that the cross-flow (axial) velocity along the module channel is constant [24].

2.4. Numerical solution procedure

The model is discretized as a set of differential and algebraic equations (DAE) with equal numbers of unknowns and solved by the Newton solver in MAPLE V Waterloo, a computer algebra system. For the solution procedure, the model is first analyzed based on the plug-flow assumptions, which implies that axial water velocity (v_z) changes with z-position but not with x-position. The performance of the membrane module is calculated by numerically solving the corresponding set of DAE, i.e., mass and volume balances, combined with transport equations, mass transfer co-relations, and pressure losses, using the finite difference method, which requires discretization of the membrane along the channel length. The performance of a pressure vessel (PV) is then determined by sequential calculation of the individual modules in this PV.

The feed channel is divided into np segments of equal intervals Δz, in which $\Delta z = L_{ch}/np$. The segments are numbered from the channel entry ($i = 0$) to the channel exit ($i = np$), with the sequential increment of $i + 1$, $i = 1..\ np$ as shown in Fig. 2. Starting with the first row of balance elements ($i = 1$) in the z-direction and using initial conditions, an initial guess for the permeate channel is performed. Then, at any position along the membrane module, pressures, concentrations, fluxes (water and salt), and velocities are computed by an iterative technique. The

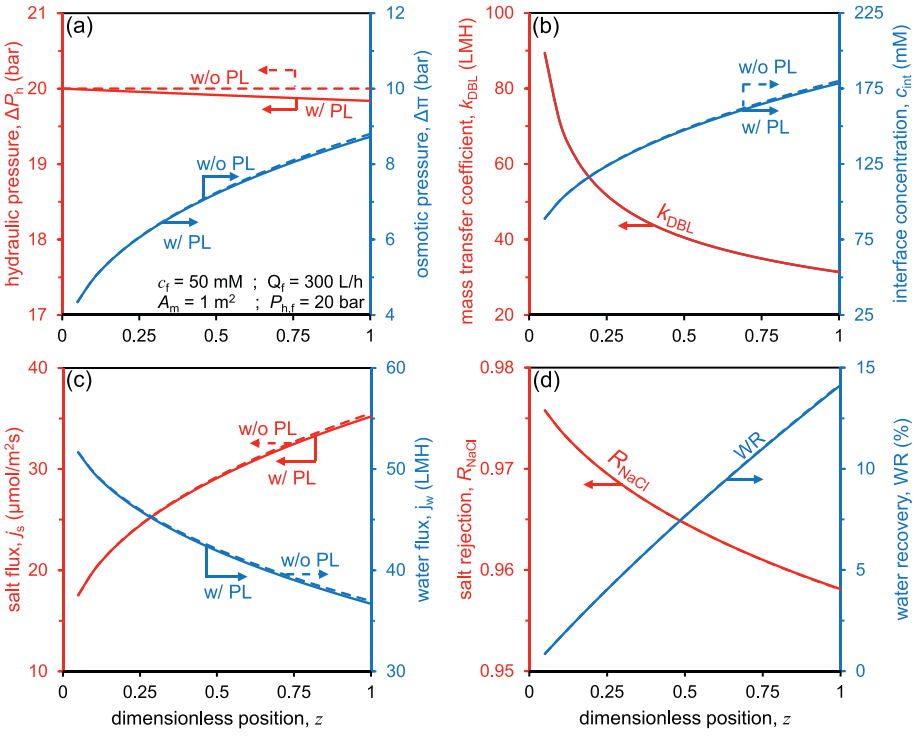

Fig. 3. Profiles of local (a) hydraulic pressure difference, osmotic pressure difference, (b) mass transfer coefficient, interface concentration, (c) salt flux, water flux, and (d) salt rejection, water recovery, along the module length (z-direction) for BWM. The dashed lines are computations for case I - without hydraulic pressure loss (w/o PL), and continuous lines are for case II - with hydraulic pressure loss (w/ PL). Feed conditions are: $Q_f = 300$ L/h, $c_f = 50$ mM, inlet feed pressure, $P_{h,f} = 20$ bar, and membrane properties are tabulated in Table 1, with the membrane length and width equated to $L_m = W_m = 1$ m.

iteration is stopped when the conditions set at the end of the feed channel are satisfied: the numerical values for two successive iterations differ in a given tolerance, i.e., 0.0001 %. The values of the feed channel conditions obtained are used as initial conditions for the next row of balance elements, and the procedure is repeated (Fig. 2).

3. Results and discussion

In this section, we discuss the trends observed in water and salt transport along the module length. We also analyze the local module performance in z-direction by evaluating the local salt rejection and water recovery. We perform these computations using modeling parameters depicted in Table 1, which relates to a study in ref. [47] for a brackish water membrane (BWM) - Dow FilmTec BW30, and a seawater membrane (SWM) - Dow FilmTec SW30-HRLE. Later, we perform parametric studies on process conditions, such as feed flow rate, hydraulic pressure, and salinity, for both BWM and SWM membrane modules and give insights into the optimal process selection. Finally, we do a performance optimization computation by varying the membrane geometry and the number of modules in a pressure vessel (PV).

3.1. Profiles along module length

First, we focus on the pressure change along the module length. The hydraulic pressure decreases with z-position on the feed channel, but the decay decreases towards the exit because v_z goes down. The opposite should be observed on the permeate channel where the hydraulic pressure drop starts slowly but then increases with z-position because v_z increases due to more water flowing through the membrane.

Using Eq. (16) with a friction coefficient of $k = 7$ [24] and a feed-flow rate of $Q_f = 300$ L/h per 1 m^2 membrane area, we compute a hydraulic pressure loss of ~0.16 bar for a 1 m long module i.e., $\Delta P_{h,0}$ - $\Delta P_{h,L_{ch}}$ ~0.16 bar. The selected value of k means that the pressure loss in a feed channel with spacers is 7 times greater than in a spacer-free feed channel. The 0.16 bar pressure loss represents typical operational conditions for a 1 m long RO module. When the hydraulic pressure loss greatly increases, the RO process efficiency may be significantly compromised. This study uses Eq. (11) to predict the feed axial velocity as a function of z-direction. By simultaneously solving Eqs. (11) and (15), we numerically ascertain the local hydraulic pressure drop profile along the module length (axial direction).

The resulting profile, depicted in Fig. 3a, is juxtaposed with the osmotic pressure change. Notably, the osmotic pressure difference marginally reduces when hydraulic pressure loss is considered, owing to the reduction in salt concentration on the feed-membrane interface as depicted in Fig. 3b. The mass transfer coefficient (k_{DBL}) decreases with z-position due to a decline of axial velocity, a parameter minimally influenced by pressure loss. Concurrently, the water flux decreases along the membrane length due to an increased salt osmotic pressure. Incorporating hydraulic pressure loss into the computation results in a marginal decrease in water flux, as illustrated in Fig. 3c, although the change is minimal. A similar marginal decline is observed for the salt flux.

When comparing the two cases, i.e., without hydraulic pressure loss (case I) and with hydraulic pressure loss (case II), we observe negligible variation in the local rejection and water recovery (Fig. 3d). Thus, we infer that the hydraulic pressure loss along the module length has an insignificant impact on a single module's local and overall performance. Based on this finding, the effect of pressure loss along module length can be neglected when modeling mass transport of a $L_m = W_m = 1$ m RO module, thereby simplifying computational efforts.

3.2. A parametric study on the module performance

To study the overall performance of an RO module, different parameters can be adjusted. In this study, we perform a parametric study on the effects of feed flow rate and feed pressure on the performance of BWM and SWM. The computation also considers the hydraulic pressure loss along the module length.

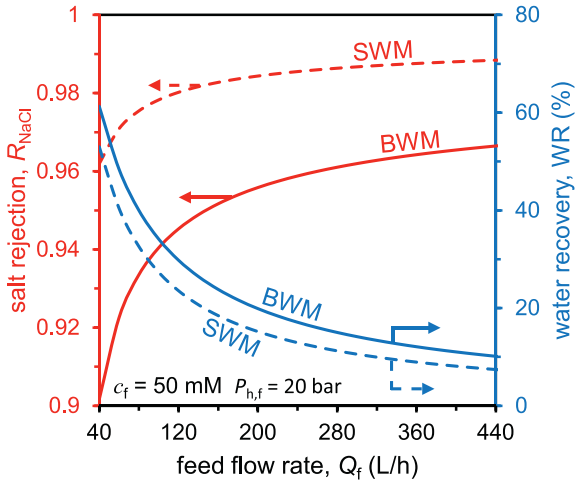

Fig. 4. Effects of feed flow rate on salt rejection and water recovery for BWM (continuous lines) and SWM (dashed lines) modules.

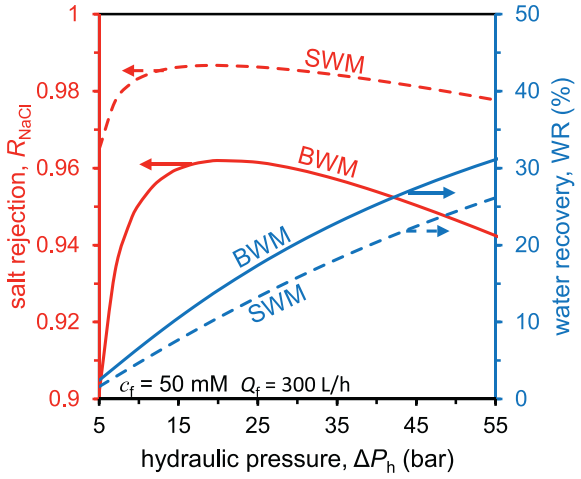

Fig. 5. Effects of hydraulic feed pressure on salt rejection and water recovery for BWM (continuous lines) and SWM (dashed lines) modules.

When the feed-flow rate is increased under a constant feed pressure, a corresponding increase in the axial velocity (v_z) ensues. This results in decreased salt concentration at the feed-membrane interface, resulting in an increased DBL mass transfer coefficient and a reduced DBL thickness (see the appendix for a detailed description). As a result, the increased DBL mass transfer coefficient reduces salt transport across the membrane, increasing rejection as seen in Fig. 4. On the other hand, with the feed pressure remaining constant, an increase in feed-flow rate marginally enhances water flux across the membrane while concurrently reducing water recovery (WR). WR is expressed as $WR = Q_p/Q_f$, where Q_p is the permeate flow rate given by $Q_p = j_w \times A_m$. The reduction of WR is attributed to higher hydraulic pressure losses in the feed channel due to an increase in axial velocity (v_z). Also, the increase in v_z decreases the osmotic pressures across the membrane due to a decrease in DBL thickness. The distinct rejection and water recovery profiles exhibited by BWM and SWM stem from the different intrinsic properties of the respective membranes, as outlined in Table 1.

The permeate productivity or the water recovery of a membrane module can be increased by either increasing the active membrane area (see Section 2 in the supporting information), increasing the water permeability coefficient, or increasing the feed pressure. In our

Table 2
Default module operational conditions unless otherwise stated.

Feed simulation conditions	
Inlet pressure, $P_{h,f}$	20 bar
Flow rate (per $A_m = 1$ m^2), Q_f	300 L/h
Temperature, T_f	25 °C
Salt concentration, c_{NaCl}	50 mM

parametric study, the water recovery increased by about 29 % (2–31 %) for BWM and 25 % (1–26 %) for SWM, with a hydraulic pressure increment of 50 bar (5–55 bar), as depicted in Fig. 5. Similarly, the salt rejection increases with hydraulic pressure. However, the effect becomes opposite above 15 bar for SWM and 20 bar for BWM. This is because the high hydraulic pressure will cause an increase in salt transport across the membrane due to the increasing DBL. The salt buildup near the membrane surface causes a concentration gradient, which reduces the effective osmotic pressure difference, making it easier for salt to move across the membrane, thus lowering rejection. Furthermore, increasing hydraulic pressure will result in an increased permeate water flux, which in turn carries solutes to the permeate, thus lowering rejection. It is important to note that a membrane module has a lower rejection under the same filtration conditions than a smaller membrane coupon. The effect of membrane area on salt rejection and water recovery is explained in the SI.

3.3. RO module performance optimization

In this subsection, we perform a series of RO optimization computations to investigate the effects of membrane geometry (length-to-width ratio for a 1 m^2 membrane sheet) on the module performance and the number of RO modules in a PV. The computations are based on the operating conditions stipulated in Table 2.

3.3.1. Membrane geometry optimization

The membrane sheet geometry greatly affects the overall RO performance. For SWRO modules, the diameter of the module is directly proportional to the membrane sheet width (W_m) due to the fact that the membrane is wrapped around the permeate collector tube. When the geometry is varied, the RO performance varies due to the hydrodynamic change of water flow in the feed channel. In this study, we vary both the membrane length and width, where we investigate the effects of membrane length to width ratio (L_m/W_m) on pressure (hydraulic and osmotic), axial velocity, and flux (salt and water) for a BWM sheet.

We note that the L_m/W_m ratio can be significantly influenced by the pressure losses in the permeate channel and the reduction of the effective membrane area due to gluing of the membrane envelope, as detailed in ref. [22]. However, these two factors were not included in the scope of this study. The membrane geometry optimization only considered pressure losses in the feed channel.

Given the assumption of a constant active surface area $A_m = 1$ m^2 for our membrane sheet, a higher value of L_m/W_m ratio signifies a comparatively elongated membrane module with a smaller diameter. This results in three notable effects: an increase in the axial velocity, an increase in hydraulic pressure loss, and a decrease in osmotic pressure difference across the membrane surface due to a reduced DBL, as illustrated in Fig. 6a. These combined effects bring about a decrease in both water and salt transport across the membrane, thereby leading to a

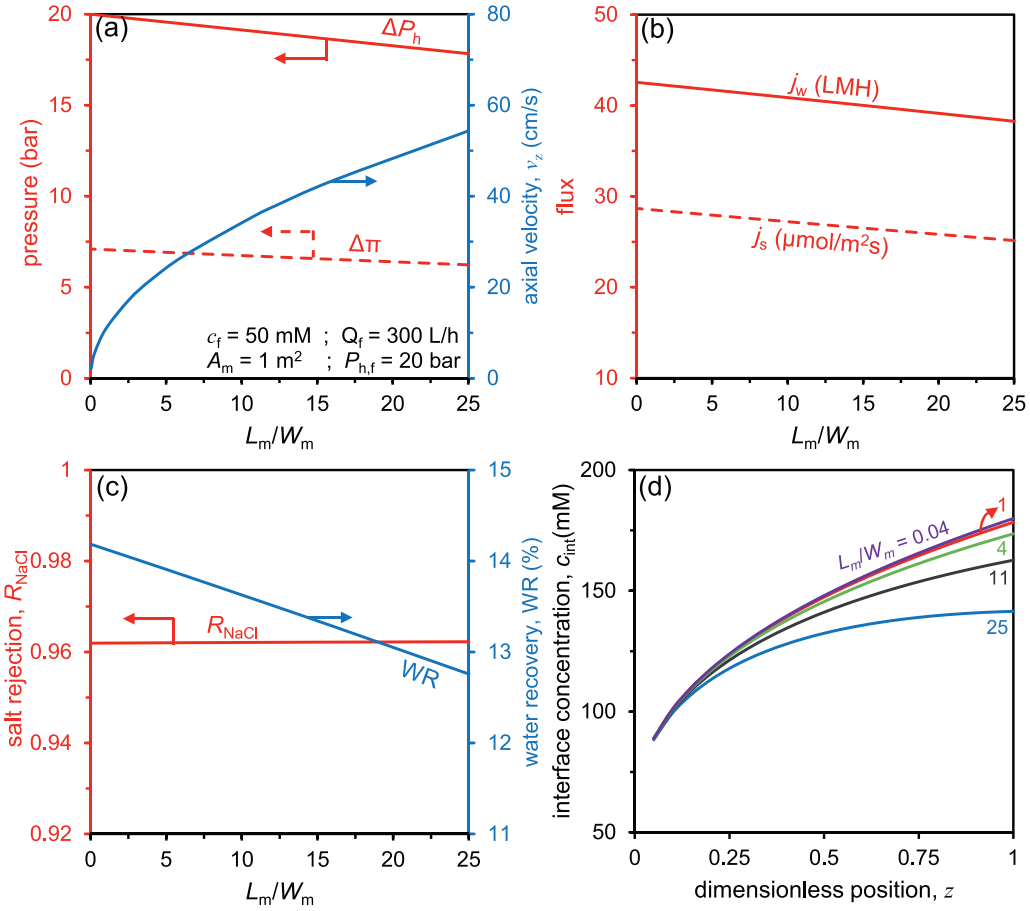

Fig. 6. Profiles showing effects of membrane length to width ratio (L_m/W_m) on (a) hydraulic pressure, osmotic pressure, axial velocity, (b) salt flux, water flux, (c) salt rejection, water recovery, and (d) concentration on the feed-membrane interface along the module length, for a 1 m^2 BWM sheet.

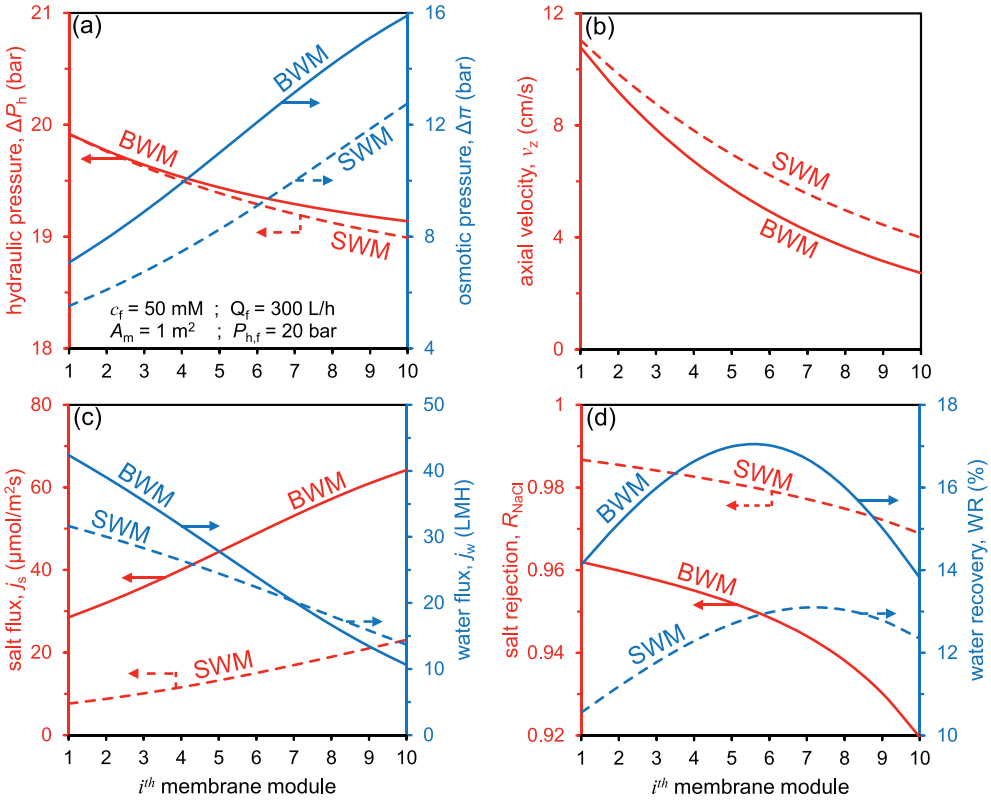

Fig. 7. Profiles of (a) pressure (hydraulic and osmotic), (b) axial velocity, (c) fluxes (salt and water), and (d) salt rejection, water recovery, for a membrane module (i^{th}) in a PV. The continuous lines are profiles for BWM, and the dashed lines are for SWM.

decline in the corresponding fluxes with increasing L_m/W_m ratio, as evidenced in Fig. 6b. This decline in water flux, in turn, results in a reduction in water recovery, as depicted in Fig. 6c. However, it is noteworthy that the salt rejection remains unaffected by the variation in the L_m/W_m ratio, which means that salt rejection is relatively insensitive to the RO membrane geometry for a constant active membrane area.

The influence of L_m/W_m on the concentration at the feed-membrane interface (c_{int}) along the dimensionless position (z-coordinate) of the module length was further examined. As the L_m/W_m ratio increases, a decrease in c_{int} is observed. As previously mentioned, a higher ratio indicates a longer module with a smaller diameter, leading to an increase in axial velocity. This increase reduces the DBL thickness, thereby resulting in a decrease in c_{int}. Fig. 6d illustrates the profiles of c_{int} with dimensionless position z along the module length.

3.3.2. *Optimization on the number of membrane modules in a pressure vessel*

The number of membrane modules in a pressure vessel (PV) significantly affects the overall water recovery and salt rejection. In this section, we consider a one-stage plant configuration under operational conditions stipulated in Table 2, with module computation involving one leaf of membrane sheet ($A_m = 1$ m^2) actively involved with filtration. In this section, we perform an example calculation for 10 module elements in a PV for enhanced visualization and analysis. However, in a real full scale installation, a PV typically houses between 3 and 7 elements.

The variation in the number of modules in relation to permeate productivity is attributed to the hydraulic pressure losses within the feed channel and the osmotic pressure differential across the membrane. As depicted in Fig. 7a, an increment in the number of modules per PV enhances hydraulic pressure loss within the feed channel. Simultaneously, there is an elevation in osmotic pressure, stemming from an increasing DBL brought about by a decreasing axial velocity, v_z, as illustrated in Fig. 7b.

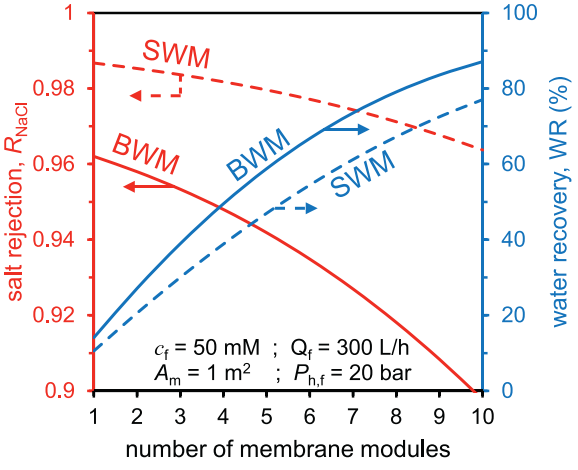

Fig. 8. Effects of the number of modules in a PV on the salt rejection and water recovery for BWM (continuous lines) and SWM (dashed lines).

As the DBL increases along the PV, the salt flux across the membrane gradually increases, reducing the overall rejection of the membrane module. Likewise, an increased hydraulic pressure loss along the PV contributes to a decline in water flux, as depicted in Fig. 7c. From our PV computation, a maximum water recovery of WR = 17.0 % was observed at the 6th membrane module for BWM, and WR = 13.1 % observed at the 7th membrane module for SWM, as illustrated in Fig. 7d. The lower water recovery or permeate productivity for SWM is due to the tighter membrane structure and thus the lower water permeability coefficient, i.e., $A_{w,SWM} < A_{w,BWM}$.

When the overall performance of the entire PV is evaluated, the

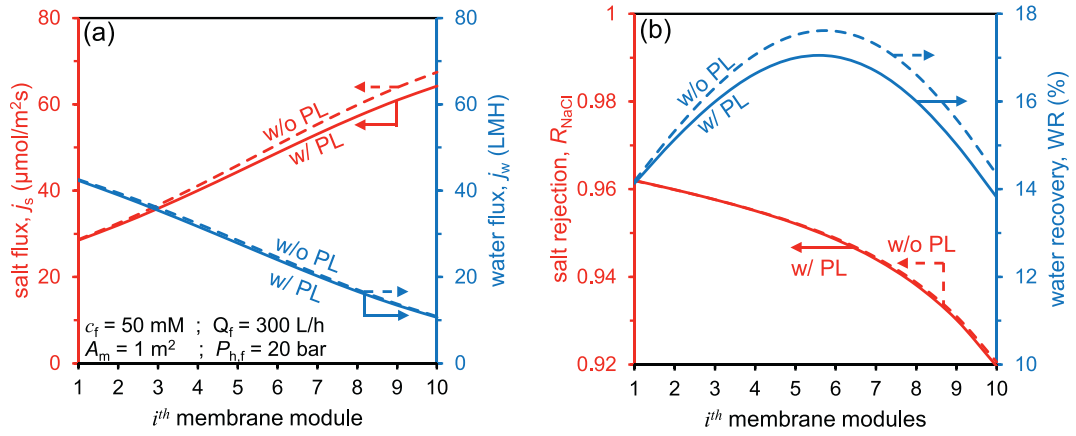

Fig. 9. Profiles showing the effects of pressure drop on the (a) salt flux, water flux, and (b) salt rejection, water recovery, for a membrane module (i^{th}) in a PV containing 10 BWM modules. The continuous lines are profiles with pressure loss (w/ PL), whereas the dashed lines are profiles without pressure loss (w/o PL).

water recovery for both BWM and SWM gradually increases with an increase in the number of membrane modules. This is despite a decrease in the water flux by the subsequent membrane modules. With the input feed conditions stated in Table 2, a PV with 10 membrane modules would give a maximum water recovery of WR = 87.1 % and WR = 77.1 % for BWM and SWM, respectively, as illustrated in Fig. 8. Conversely, a rejection drop of ΔR_{NaCl} = 4.2 % (96.2–92.0 %) and ΔR_{NaCl} = 1.8 % (98.7–96.9 %) is observed for BWM and SWM respectively.

The effect of hydraulic pressure loss on the performance of RO membrane modules arranged within a PV is illustrated in Fig. 9. With an increment in the number of membrane modules within a PV, there is a corresponding increase in salt flux attributable to the expanding DBL. In contrast, disregarding pressure loss along the module length leads to a more pronounced increment in salt flux, primarily driven by increased water flux (Fig. 9a). Nonetheless, the resultant change in the overall salt rejection of the whole module remains relatively modest, as depicted in Fig. 9b. Notably, the model prediction significantly impacts water recovery per membrane module. In the absence of pressure loss effects, an optimal water recovery of WR = 17.6 % was observed at the 6th membrane module, signifying an increment of 0.6 % from WR = 17.0 % when hydraulic pressure loss is considered.

4. Conclusions

In this study, a two-dimensional (2D) mass transport model for a reverse osmosis (RO) module is developed using the solution friction (SF) theory, which includes intrinsic membrane properties. The novelty lies in using SF theory, which incorporates the charge and solute transport factors, which have not been used in existing 2D models. Integrating mass and volume balances facilitates deriving an effective numerical solution spanning the entire module length. Our analysis studies both local and whole module performance, revealing a minimal impact of hydraulic pressure loss on the performance of a single module. Nonetheless, the significance of pressure loss becomes pronounced when considering a pressure vessel (PV) with several membrane modules.

We present opportunities to optimize module performance through a systematic parametric study, which includes varying feed conditions, membrane geometry, and the number of modules in a PV. For a given membrane type and a set of feed variables, our 2D SF model can predict the module with the maximum water recovery (WR) in a PV. Our modeling framework has the potential to create an optimal staging profile based on salt rejection and permeate productivity, therefore enhancing RO plant operational efficiency and performance.

Although this study gives a detailed 2D computational prediction for an RO module, it is important to accurately model all flows and pressure profiles, including those in the permeate channel. By doing so, a more comprehensive RO module performance. 2D model prediction output can be used to optimize the RO module performance accurately and better. Therefore, future work can include pressure losses in the permeate channel and the module performance compared with the findings of this study.

Glossary and symbols

Acronyms

BWM	Brackish water membrane
DBL	Diffusion boundary layer
DSPM	Donnan steric partitioning pore model
NPE	Nernst-Planck eq.
PV	Pressure vessel
RO	Reverse osmosis
SD	Solution-diffusion
SF	Solution-friction
SWM	Seawater membrane
SWRO	Spiral wound reverse osmosis
TMP	Trans-membrane pressure
WR	Water recovery

Symbols

$\Delta\Pi$	Trans-membrane osmotic pressure (bar)
ΔP_h	Trans-membrane hydraulic pressure (bar)
δ_m	Membrane thickness (m)
η	Dynamic viscosity of solution (Pa·s)
γ	Shear rate (s^{-1})
ϕ	Electrical potential (V)
Φ_s	Salt partitioning coefficient (−)
σ	Salt reflection coefficient (−)
ε_m	Mass transport reduction factor (−)
A_{ch}	Feed channel axial flow area (m^2)
A_m	Active membrane area (m^2)
A_w	Water permeability coefficient (LMH/bar)
B_s	Salt permeability coefficient (LMH)
C	Charge factor (mol/m^3)
c_f	Salt concentration on the feed side of the membrane (mol/m^3)
c_{int}	Salt concentration on the feed-membrane interface (mol/m^3)
c_p	Salt concentration on the permeate side of the membrane (mol/m^3)
$D_{\infty,s}$	Bulk diffusion coefficient of salt in water (m^2/s)
F	Faraday constant (C/mol)
F_c	Flux conversion factor (3.6×10^6)

H_{ch}	Channel height (m)
J_s	Trans-membrane salt flux (mol/m^2/s)
J_w	Trans-membrane water flux (LMH)
k	Friction coefficient due to spacer geometry (−)
$k_{DBL,s}$	Salt mass transfer coefficient in the DBL (LMH)
$K_{f,s}$	Salt friction coefficient due to membrane matrix (−)
$k_{m,s}$	Salt mass transfer coefficient in the membrane (LMH)
L_{ch}	Channel length (m)
P_c	Pressure conversion factor (10^5)
P_{st}	Static pressure (bar)
P_s	Salt transport factor (LMH)
Q_f	Feed volumetric flow rate (m^3/s)
Q_p	Permeate volumetric flow rate (m^3/s)
R	Gas constant (J/mol/K)
R_s	Salt rejection (−)
T	Temperature (K)
v_x	Trans-membrane flow velocity (m/s)
v_z	Cross-flow or axial velocity (m/s)
W_{ch}	Channel width (m)
X_m	Membrane charge density (mol/m^3)

CRediT authorship contribution statement

All authors contributed equally to this work.

Declaration of competing interest

The authors declare that they have no known competing financial interests or personal relationships that could have appeared to influence the work reported in this paper.

Acknowledgements

This work was performed in the cooperation framework of Wetsus, *European Centre of Excellence for Sustainable Water Technology* (www.wetsus.nl). Wetsus is co-funded by the Dutch Ministry of Economic Affairs and Ministry of Infrastructure and Environment, the Province of Fryslán, and the Northern Netherlands Provinces. The authors thank the participants in the Wetsus research theme, Advanced Water Treatment, for fruitful discussions and financial support. S. Porada acknowledges financial support from the Polish National Agency for Academic Exchange - Polish Returns Grant (BPN/PPO/2021/1/00010).

Appendix A. Supplementary data

Supplementary data to this article can be found online at https://doi.org/10.1016/j.desal.2024.118429.

Data availability

The research data underlying this work is available at data repository - https://doi.org/10.4121/83df4d6e-26a4-44a4-8913-e185ba01ebec.

References

[1] Y. Marcus, A simple empirical model describing the thermodynamics of hydration of ions of widely varying charges, sizes, and shapes, Biophys. Chem. 51 (2–3) (1994) 111–127.
[2] E.R. Nightingale Jr., Phenomenological theory of ion solvation. Effective radii of hydrated ions, J. Phys. Chem. 63 (9) (1959) 1381–1387.
[3] X. Zhang, D.G. Cahill, O. Coronell, B.J. Mariñas, Partitioning of salt ions in FT30 reverse osmosis membranes, Appl. Phys. Lett. 91 (18) (2007).
[4] R. Epsztein, R.M. DuChanois, C.L. Ritt, A. Noy, M. Elimelech, Towards single-species selectivity of membranes with subnanometre pores, Nat. Nanotechnol. 15 (6) (2020) 426–436.
[5] C. Lu, C. Hu, C.L. Ritt, X. Hua, J. Sun, H. Xia, Y. Liu, D.-W. Li, B. Ma, M. Elimelech, et al., In situ characterization of dehydration during ion transport in polymeric nanochannels, J. Am. Chem. Soc. 143 (35) (2021) 14242–14252.
[6] L. Wang, T. Cao, K.E. Pataroque, M. Kaneda, P.M. Biesheuvel, M. Elimelech, Significance of co-ion partitioning in salt transport through polyamide reverse osmosis membranes, Environ. Sci. Technol. 57 (9) (2023) 3930–3939.
[7] P.M. Biesheuvel, L. Zhang, P. Gasquet, B. Blankert, M. Elimelech, W.G.J. van der Meer, Ion selectivity in brackish water desalination by reverse osmosis: theory, measurements, and implications, Environ. Sci. Technol. Lett. 7 (1) (2019) 42–47.
[8] L. Zhang, P.M. Biesheuvel, I.I. Ryzhkov, Theory of ion and water transport in electron-conducting membrane pores with pH-dependent chemical charge, Phys. Rev. Appl. 12 (1) (2019) 014039.
[9] E. M. Kimani, A. J. B. Kemperman, W. G. J. van der Meer, P. M. Biesheuvel, Multicomponent mass transport modeling of water desalination by reverse osmosis including ion pair formation, The Journal of chemical physics 154 (12).
[10] M.M. Zubair, H. Saleem, S.J. Zaidi, Recent progress in reverse osmosis modeling: an overview, Desalination 564 (2023) 116705.
[11] K. Kezia, J. Lee, W. Ogieglo, A. Hill, N.E. Benes, S.E. Kentish, The transport of hydronium and hydroxide ions through reverse osmosis membranes, J. Membr. Sci. 459 (2014) 197–206.
[12] Y.S. Oren, P.M. Biesheuvel, Theory of ion and water transport in reverse-osmosis membranes, Phys. Rev. Appl. 9 (2) (2018) 024034.
[13] P.M. Biesheuvel, J.E. Dykstra, Physics of Electrochemical Processes, 2020.
[14] P.M. Biesheuvel, S. Porada, M. Elimelech, J.E. Dykstra, Tutorial review of reverse osmosis and electrodialysis, J. Membr. Sci. 647 (2022) 120221.
[15] P. Läuger, Transport phenomena in membranes, Angew. Chem. Int. Ed. Eng. 8 (1) (1969) 42–54.
[16] W.R. Bowen, A.W. Mohammad, N. Hilal, Characterisation of nanofiltration membranes for predictive purposes—use of salts, uncharged solutes and atomic force microscopy, J. Membr. Sci. 126 (1) (1997) 91–105.
[17] G. Hagmeyer, R. Gimbel, Modelling the rejection of nanofiltration membranes using zeta potential measurements, Sep. Purif. Technol. 15 (1) (1999) 19–30.
[18] K. Kezia, J. Lee, A.J. Hill, S.E. Kentish, Convective transport of boron through a brackish water reverse osmosis membrane, J. Membr. Sci. 445 (2013) 160–169.
[19] L. Zhang, H.V.M. Hamelers, P.M. Biesheuvel, Modeling permeate pH in RO membranes by the extended donnan steric partitioning pore model, J. Membr. Sci. 613 (2020) 118511.
[20] E.M. Kimani, M. Pranić, S. Porada, A.J.B. Kemperman, I.I. Ryzhkov, W.G.J. van der Meer, P.M. Biesheuvel, The influence of feedwater pH on membrane charge ionization and ion rejection by reverse osmosis: an experimental and theoretical study, J. Membr. Sci. 660 (2022) 120800.
[21] J. Park, K.S. Lee, A two-dimensional model for the spiral wound reverse osmosis membrane module, Desalination 416 (2017) 157–165.
[22] W.G.J. van der Meer, J.C. van Dijk, Theoretical optimization of spiral-wound and capillary nanofiltration modules, Desalination 113 (2–3) (1997) 129–146.
[23] G. Guillen, E.M.V. Hoek, Modeling the impacts of feed spacer geometry on reverse osmosis and nanofiltration processes, Chem. Eng. J. 149 (1–3) (2009) 221–231.
[24] L. Song, S. Hong, J.Y. Hu, S.L. Ong, W.J. Ng, Simulations of full-scale reverse osmosis membrane process, J. Environ. Eng. 128 (10) (2002) 960–966.
[25] A.E. Anqi, N. Alkhamis, A. Oztekin, Computational study of desalination by reverse osmosis—three-dimensional analyses, Desalination 388 (2016) 38–49.
[26] S. Cespedes, F.D. Martinez, F. Salto-Quintana, B. Blankert, C. Picioreanu, Three-dimensional concentration-polarization modeling of trace-ions in reverse osmosis, J. Membr. Sci. 693 (2024) 122349.
[27] M. Li, T. Bui, S. Chao, Three-dimensional CFD analysis of hydrodynamics and concentration polarization in an industrial RO feed channel, Desalination 397 (2016) 194–204.
[28] A.I. Radu, L. Bergwerff, M.C.M. Van Loosdrecht, C. Picioreanu, A two-dimensional mechanistic model for scaling in spiral wound membrane systems, Chem. Eng. J. 241 (2014) 77–91.
[29] M.A. Junker, W.M. de Vos, R.G.H. Lammertink, J. de Grooth, Bridging the gap between lab-scale and commercial dimensions of hollow fiber nanofiltration membranes, J. Membr. Sci. 624 (2021) 119100.
[30] L. Song, M. Heiranian, M. Elimelech, True driving force and characteristics of water transport in osmotic membranes, Desalination 520 (2021) 115360.
[31] L. Wang, J. He, M. Heiranian, H. Fan, L. Song, Y. Li, M. Elimelech, Water transport in reverse osmosis membranes is governed by pore flow, not a solution-diffusion mechanism, science, Advances 9 (15) (2023) eadf8488.
[32] E.P. Chan, B.R. Frieberg, K. Ito, J. Tarver, M. Tyagi, W. Zhang, E.B. Coughlin, C. M. Stafford, A. Roy, S. Rosenberg, C.L. Soles, Insights into the water transport mechanism in polymeric membranes from neutron scattering, Macromolecules 53 (4) (2020) 1443–1450.
[33] O. Kedem, A. Katchalsky, Thermodynamic analysis of the permeability of biological membranes to non-electrolytes, Biochim. Biophys. Acta 27 (1958) 229–246.
[34] Y. Roy, J.H. Lienhard, On the presence of solute-solvent transport coupling in reverse osmosis, J. Membr. Sci. 611 (2020) 118272.
[35] E.-S. Jang, W. Mickols, R. Sujanani, A. Helenic, T.J. Dilenschneider, J. Kamcev, D. R. Paul, B.D. Freeman, Influence of concentration polarization and thermodynamic non-ideality on salt transport in reverse osmosis membranes, J. Membr. Sci. 572 (2019) 668–675.
[36] A.P. Straub, C.O. Osuji, T.Y. Cath, M. Elimelech, Selectivity and mass transfer limitations in pressure-retarded osmosis at high concentrations and increased operating pressures, Environ. Sci. Technol. 49 (20) (2015) 12551–12559.
[37] H. Fan, M. Heiranian, M. Elimelech, The solution-diffusion model for water transport in reverse osmosis: what went wrong? Desalination 580 (2024) 117575.
[38] L. Yao, Y. Li, Q. Cheng, Z. Chen, J. Song, Modeling and optimization of metal-organic frameworks membranes for reverse osmosis with artificial neural networks, Desalination 532 (2022) 115729.

[39] A. Ruiz-García, I. Nuez, M. Khayet, Performance assessment and modeling of an SWRO pilot plant with an energy recovery device under variable operating conditions, Desalination 555 (2023) 116523.
[40] N.I. Ajali-Hernández, A. Ruiz-García, C.M. Travieso-González, ANN based-model for estimating the boron permeability coefficient as boric acid in swro desalination plants using ensemble-based machine learning, Desalination 573 (2024) 117180.
[41] A. Mohammed, H. Alshraideh, F. Alsuwaidi, A holistic framework for improving the prediction of reverse osmosis membrane performance using machine learning, Desalination 574 (2024) 117253.
[42] D. Gaublomme, W. Quaghebeur, A. Van Droogenbroeck, M. Vanoppen, B. De Gusseme, A. Verliefde, I. Nopens, E. Torfs, A hybrid modelling approach for reverse osmosis processes including fouling, Desalination 564 (2023) 116756.
[43] W. Quaghebeur, E. Torfs, B. De Baets, I. Nopens, Hybrid differential equations: integrating mechanistic and data-driven techniques for modelling of water systems, Water Res. 213 (2022) 118166.
[44] M. Von Stosch, R. Oliveira, J. Peres, S.F. de Azevedo, Hybrid semi-parametric modeling in process systems engineering: past, present and future, Comput. Chem. Eng. 60 (2014) 86–101.
[45] S. Al Aani, T. Bonny, S.W. Hasan, N. Hilal, Can machine language and artificial intelligence revolutionize process automation for water treatment and desalination? Desalination 458 (2019) 84–96.
[46] M.Y. Schneider, W. Quaghebeur, S. Borzooei, A. Froemelt, F. Li, R. Saagi, M. J. Wade, J.-J. Zhu, E. Torfs, Hybrid modelling of water resource recovery facilities: status and opportunities, Water Sci. Technol. 85 (9) (2022) 2503–2524.
[47] P.M. Biesheuvel, S.B. Rutten, I.I. Ryzhkov, S. Porada, M. Elimelech, Theory for salt transport in charged reverse osmosis membranes: novel analytical equations for desalination performance and experimental validation, Desalination 557 (2023) 116580.
[48] K.S. Spiegler, O. Kedem, Thermodynamics of hyperfiltration (reverse osmosis): criteria for efficient membranes, Desalination 1 (4) (1966) 311–326.
[49] S. De, P.K. Bhattacharya, Prediction of mass-transfer coefficient with suction in the applications of reverse osmosis and ultrafiltration, J. Membr. Sci. 128 (2) (1997) 119–131.
[50] P. M. Biesheuvel, S. Porada, B. Blankert, I. Ryzhkov, M. Elimelech, Analysis of concentration polarization in reverse osmosis and nanofiltration: zero-, one-, and two-dimensional models, arXiv preprint arXiv:2401.11527 (2024).
[51] M. Heiranian, H. Fan, L. Wang, X. Lu, M. Elimelech, Mechanisms and models for water transport in reverse osmosis membranes: history, critical assessment, and recent developments, Chem. Soc. Rev. 52 (2023) 8455–8480, https://doi.org/10.1039/D3CS00395G.
[52] F.D. Martinez-Jimenez, V.-E. Musteata, S. Cespedes-Zuluaga, B. Blankert, C. Picioreanu, Two-dimensional model of ion transport in composite membranes active layers with tem-scanned morphology, Desalination 565 (2023) 116876.
[53] C.R. Bouchard, P.J. Carreau, T. Matsuura, S. Sourirajan, Modeling of ultrafiltration: predictions of concentration polarization effects, J. Membr. Sci. 97 (1994) 215–229.
[54] A.S. Berman, Laminar flow in channels with porous walls, J. Appl. Phys. 24 (9) (1953) 1232–1235.
[55] A. Ruiz-García, I. Nuez, A time-dependent model of pressure drop in reverse osmosis spiral wound membrane modules, IFAC-PapersOnLine 54 (3) (2021) 158–163.
[56] G. Schock, A. Miquel, Mass transfer and pressure loss in spiral wound modules, Desalination 64 (1987) 339–352.
[57] A. Ruiz-García, I. Nuez, Performance assessment of SWRO spiral-wound membrane modules with different feed spacer dimensions, Processes 8 (6) (2020) 692.
[58] Z. Han, M. Terashima, B. Liu, H. Yasui, CFD investigation of the effect of the feed spacer on hydrodynamics in spiral wound membrane modules, Math. Comput. Appl. 23 (4) (2018) 80.
[59] H.S. Abid, D.J. Johnson, R. Hashaikeh, N. Hilal, A review of efforts to reduce membrane fouling by control of feed spacer characteristics, Desalination 420 (2017) 384–402.
[60] A. Haidari, S. Heijman, W. Van Der Meer, Optimal design of spacers in reverse osmosis, Sep. Purif. Technol. 192 (2018) 441–456.
[61] P. Xie, L.C. Murdoch, D.A. Ladner, Hydrodynamics of sinusoidal spacers for improved reverse osmosis performance, J. Membr. Sci. 453 (2014) 92–99.
[62] C. Koutsou, S. Yiantsios, A. Karabelas, Direct numerical simulation of flow in spacer-filled channels: effect of spacer geometrical characteristics, J. Membr. Sci. 291 (1–2) (2007) 53–69.